

ULTRA-HIGH ENERGY COSMIC-RAY ACCELERATION IN THE JET OF CENTAURUS A

MITSURU HONDA

Plasma Astrophysics Laboratory, Institute for Global Science, Mie, Japan
Draft version November 12, 2018

ABSTRACT

We evaluate the achievable maximum energy of nuclei diffusively accelerated by shock wave in the jet of Cen A, based on an updated model involving the stochastic magnetic fields that are responsible for recent synchrotron X-ray measurements. For the maximum energy analysis, conceivable energy constraints from spatiotemporal scales are systematically considered for the jet-wide including discrete X-ray knots. We find that in the inner region within ~ 1 arcmin from galactic core, which includes knots AX and BX, proton and iron nucleus can be accelerated to 10^{19} – 10^{20} and 10^{21} eV (10–100 EeV and ZeV) ranges, respectively. The upper cutoff energy of the very energetic neutrinos produced via photopion interaction is also provided. These are essential for identifying the acceleration site of the ultra-high energy cosmic ray detected in the Pierre Auger Observatory, which signifies the arrival from nearby galaxies including Cen A.

Subject headings: acceleration of particles — galaxies: individual (Cen A) — galaxies: jets — magnetic fields — methods: analytical — turbulence

1. INTRODUCTION

To date, the 27 ultra-high energy cosmic ray (UHECR) events of the energy exceeding 5.7×10^{19} eV have been detected in state-of-the-art Auger observatory; in particular, the anisotropy and significant correlation with the active galactic nuclei (AGNs) residing within 75 Mpc, namely GZK horizon (Greisen 1966; Zatsepin & Kuzmin 1966), were discovered (Abraham et al. 2007). Surprisingly, the results indicate that two of these UHECR events have arrived within 3° of Centaurus A (NGC 5128), a closest galaxy (3.7 Mpc from us; Ferrarese et al. 2007). Although the detailed position of the UHECR production site is still unresolved, the galactic core accompanied by a supermassive black hole, bipolar jets, giant radio lobes (Hardcastle et al. 2009), and so on, will be enumerated as the favored candidates. It is desired that genuine theoretical survey be expanded for clarifying the particle acceleration mechanism feasible at these sites, in order to provide the physical interpretation of the observed intriguing results, which include the recent detection of high-energy gamma rays (Aharonian et al. 2009).

When closely looking at the anatomy of the large-scale jets in the Cen A galaxy (see, Israel 1998, for a review), a clue to solve this challenging problem seems to be in the knotty regions resolved in a deep X-ray image (e.g., Kraft et al. 2002). In an inner region near the galactic core, the rugged features are associated with the shocks, which are considered to be formed where a flowing plasma collides with obstacles (Hardcastle et al. 2007). According to the latest theory of plasma kinetic transport, it is known that such a colliding plasma is likely unstable for the electromagnetic current filamentation instability, which generates small-scale magnetic fluctuations with the order of plasma skin depth (Medvedev & Loeb 1999; Honda 2004 and references therein). In the nonlinear phase, the filaments preferentially coalesce one another, self-organizing larger scale filaments with stronger magnetic fields. This reflects a stochastic nature of the in-

verse energy cascade of plasma turbulence. The magnetic fluctuations are non-perturbative, and in the strong turbulence regime, in that the energy density is comparable to the thermal energy density of plasma bulk (Honda et al. 2000a,b).

Indeed, recent high-resolution observations reveal that the jet of Cen A is in part dominated by the filamentary, sometimes edge-brightened features (Hardcastle et al. 2007), as inspected in the well-confirmed jet of a nearby galaxy (Vir A; Owen et al. 1989). Worth noting thing is that inherent inner structure similar to these has been discovered in many other jets (e.g., Cyg A: Perley et al. 1984; 3C 353: Swain et al. 1998; 3C 273: Lobanov & Zensus 2001; 3C 438: Treichel et al. 2001; Mrk 501: Piner et al. 2009). Also, it was recently found that a filamentary jet model naturally provides the comprehensive explanation for the complicated spectral variability observed in a TeV blazar object (Mrk 421; Honda 2008). These ingredients strongly encourage us to take the inhomogeneous magnetic field effects into account for precisely modeling the Cen A jet as a cosmic-ray accelerator.

For a standard, diffusive shock acceleration (DSA) scenario (e.g., Blandford & Eichler 1987), the strong turbulence plays an essential role in particle scatterers is expected. In the stochastic medium, the higher energy heavy particles tend to freely meander (Honda & Honda 2005), albeit electrons (and positrons) are, if anything, likely gyro-trapped in the magnetized filaments, suffering stronger radiative cooling (Section 3.1). From the fact that in the Cen A jet, electron synchrotron emissions appear to be, in part, already diffusive, it is thus inferred that for nuclei (say, proton) the conventional approximation of small-angle resonant scattering will be inadequate for describing the spatial diffusion, and instead, the three-dimensional rms deflection becomes rather feasible. Importantly, the latter facilitates the back and forth of particles across the shock, increasing the efficiency of DSA. Based on this notion, Honda & Honda (2004) have argued that a nucleus could be accelerated to the UHE range at a bright jet knot of Vir A, though the

arrival from the galaxy (~ 4 times more distant than the distance to Cen A) is not yet signified (see, e.g., Stanev 2008, for the useful discussions).

Besides, the bound electrons are co-accelerated, to emit the synchrotron photons, which could serve as a target of the accelerated protons. Then, the resonant interaction of the UHE protons with the target photons could be a major neutrino production process via the decay channels triggered by photopionization: $p\gamma \rightarrow \pi^\pm X \rightarrow \mu^\pm \nu_\mu \rightarrow e^\pm \nu_e \nu_\mu$ (Romero et al. 1996). The emitted neutrinos propagate on the straight, unlike the charged particles that suffer, more or less, deflection by intergalactic magnetic fields (e.g., Vallée 2004), so that they play the role of a powerful and complementary messenger of the UHECR production, in light of the observability at a forthcoming kilometer neutrino telescope (e.g., Halzen & Hooper 2002). Recently, Cuoco & Hannestad (2008) have proposed the model spectra of high-energy neutrinos from Cen A, but putting the detailed mechanisms of the particle accelerator into effect has remained unsolved.

In this paper, based on the filament model, we estimate the maximum possible energies of a proton and iron diffusively accelerated in the Cen A jet, and also, the energy of the produced neutrinos, providing the energy-equipartition among the flavors. The conceivable mechanisms of the energy restriction are taken into consideration for the jet wide including bright knots. It is addressed that the energy is limited dominantly by the shock operation time or particle escape loss, rather than radiative loss and nucleus–nucleus collision timescales. As a result, we find that in the inner region, which contains the X-ray knots BX n , proton and iron can be accelerated beyond the Auger limit. In particular, the expected highest energy reaches, for iron, 3 ZeV and more (around knot BX5); that is to say, the Cen A jet is a "Zevatron" worthy of the candidate (in addition to the Vir A, put forth by Honda & Honda (2004)).

The present analysis virtually provides a substantially extended version of the previous simple analysis by Romero et al. (1996), and hence, a particular attention has been paid to highlight the new points including (1) the proposal of the improved theoretical model compatible with updated X-ray measurements (Section 2.1) and extended arguments on the turbulent magnetic field (Section 2.2), (2) the non-resonant diffusion scenario involved in the DSA (Section 3.1), and (3) thorough survey of the temporal (Section 3.2) and spatial (Section 3.3) limits, in order to figure out the maximum energies of proton and iron achievable in the inner region (Section 3.4), and estimate neutrino energy (Section 3.5). The application of the maximum energy analysis to the outer region of the large-scale jet is also provided (Section 4). At last, the discussion on the comparison with the previous relevant results is expanded (Section 5).

2. JET WIDE AS A CANDIDATE UHECR FACTORY

2.1. *The Kinematic and Spectral Properties*

Cen A is a giant elliptical galaxy (classified as Fanaroff–Riley (FR) type-I), which contains the bipolar jets ejected from the galactic core. The brighter jet extends toward the northeast direction beyond the projection of $\theta_{\text{proj}} \simeq 250''$ ($\theta_{\text{proj}} = 1''$ corresponds to 17 pc; Hardcastle et al. 2007), with its inclination with respect to the line

of sight (the angle is referred to as the viewing angle, throughout). The apparent speed of motion is subluminal, exhibiting around $0.5c$, where c is the speed of light (Hardcastle et al. 2003, 2006; Horiuchi et al. 2006; Brookes et al. 2006). Concerning the knots distributing along the jet, a model in which they are simply compressions in the fluid flow has been ruled out; and instead, they are considered to be privileged sites for the in situ particle acceleration (see, Hardcastle et al. 2003, for a detailed discussion). Although the velocity distribution inside the knot-like features is still not revealed, the knots may trace the stationary shocks, which could be formed as a result of interaction between the jet fluid and internal obstacles (Blandford & Königl 1979a,b). For updated spectral indices around $\alpha_r \simeq 0.7$ in observed radio and radio-infrared continuum (Brookes et al. 2006), we read off the energy spectral index of energetic electrons of $p = 2\alpha_r + 1 = 2.4$. The radiation spectrum extending to the X-ray band is considered to be of the electron-synchrotron originator, which contains a key information to understand the real mechanism of the accelerator that simultaneously operates for ions, as long as ion abundance is finite in the jet interior (e.g., Evans et al. 2004; Markowitz et al. 2007). In this sense, below we deal with somewhat more details of the X-ray spectrum.

Recent *Chandra* observations have successfully resolved the X-ray knots smaller than the width of the radio-emitting column with diffuse X-ray emissions (Kraft et al. 2002; Hardcastle et al. 2007), although the inner structure of the knots remains unresolved as yet. When the filamentary morphology inspected in the jet (introduced in Section 1) retains a self-similar characteristic (Honda 2008), the magnification of the spatial scale of the X-ray knots could repetitiously reveal the composition of smaller scale compactors and diffuse emitters. If this insight is correct, the DSA property is incurred by the filamentary turbulent state (Honda & Honda 2004, 2005). Considering a similar situation that allows for magnetized filamentation, Spitkovsky (2008) have verified that the energy gains truly occur as particles bounce between the upstream and downstream regions of a collisionless shock, and found $p = 2.4 \pm 0.1$, amenable to the aforementioned value.

According to the argument expanded by Honda & Honda (2007), the dominant synchrotron emissions (around the spectral break of $\sim 10^{14}$ Hz) are from the major electrons bound to the magnetized filaments with the maximum transverse size (i.e., the maximum coherence length). The electrons in smaller scale filaments down to a certain characteristic scale λ_c can be accelerated to higher energy, because of the weaker synchrotron loss in the weaker magnetic fields. In fine filaments smaller than λ_c , electron acceleration is limited by the escape from the filaments.¹ It is pointed out that the free electrons meandering in the magnetized filaments contribute to engender diffuse synchrotron photons (in the fundamental process). Anyhow, it follows that the spatial size scales of filaments are identified with the local maximum electron energies. In this context, particularly,

¹ Note here that this elementary process does *not* mean the escape (in meaning often said) from an entire system for particle confinement, like a jet column. The latter is considered in Section 3.3.

TABLE 1
SUMMARY OF THE PARAMETER VALUES

Region	$L_{\text{proj}}(\text{pc})^{\text{a}}$	$R(\text{pc})^{\text{a}}$	$R_{\text{out}}(\text{pc})^{\text{a}}$	$B_{\text{eq},\delta=1}(\mu\text{G})^{\text{b}}$	β^{c}
AX1	260	352	819	260	5/3
AX2	310	352	819	250	5/3
AX3	430	352	819	290	5/3
AX4	480	352	819	230	5/3
BX2	980	819	1310	160	5/3
BX5	1100	819	1310	290	5/3

^acf. Kraft et al. (2002).

^bEquipartition values excluding the beaming effects (cf. Section 2.2).

^cThe spectral index of the filamentary turbulence (cf. Section 2.1).

it appears that the electron synchrotron emissions from the major part, larger than λ_c , dominantly contribute to constitute an extended (typically X-ray) continuum of spectral energy distribution, instead of sharp cutoff. Taking into account of the flux density reduction due to the weak magnetic intensity, we can evaluate the F_ν spectral index above the break frequency, to give

$$\alpha_x = \frac{(5\beta - 1)p - (\beta + 3)}{2(3\beta + 1)}, \quad (1)$$

where β corresponds to the filamentary turbulent spectral index. Here, we have assumed the Kolmogorov-type fluctuations superimposing on the local magnetic fields involved in the filaments. In Equation (1), we find that, for $p = 2.4$, the values of $\beta = 5/3$, 2, and 3 (suggested by Honda (2008)) lead to $\alpha_x = 1.1$, 1.2, and 1.4, respectively. Interestingly, these are accommodated with the measured values of both $\alpha_x = 1.00^{+0.16}_{-0.15}$ in between knots A2 and B included in the projection of $\theta_{\text{proj}} \leq 60''$ (Kataoka et al. 2006) and $\alpha_x = 1.2 \pm 0.2$ in $60'' < \theta_{\text{proj}} < 190''$ (Hardcastle et al. 2007).

2.2. Turbulent Magnetic Fields

It is expected that the magnetic field vectors are almost randomly oriented inside the jet, and as is, the synchrotron radiation tends to be diffuse with the reduced polarization, with exception for that from the electrons bound to a pronounced coherent field. The field strength might be appropriately characterized by the rms value (denoted simply as B ; Honda & Honda 2005), although it is hard to directly determine the exact value from integrating the turbulent spectral intensity over the jet wide. For simplicity, we here compare it with an equipartition value. Considering the emitting volume with the size of $\sim 10''$ (Kraft et al. 2002; Hardcastle et al. 2006) that is larger than the size supposed by Kataoka & Stawarz (2005), we infer that the typical field strength may be represented by 100 μG in the inner region including bright knots A and B, and less in the outer region (Hardcastle et al. 2006). In Table 1, the revised equipartition value, denoted as $B_{\text{eq},\delta=1}$, for the simple case taking no relativistic beaming effect into account is listed. The energy density levels (u_m) are thought of as being larger than (or, at least comparable to) the radiation energy density (u_{rad}) (cf. Bai & Lee 2001).

In the radial edge of the jet, uncanceled magnetic fields in the envelope of the clustered filaments cooperate to apparently constitute a long magneto-tail ex-

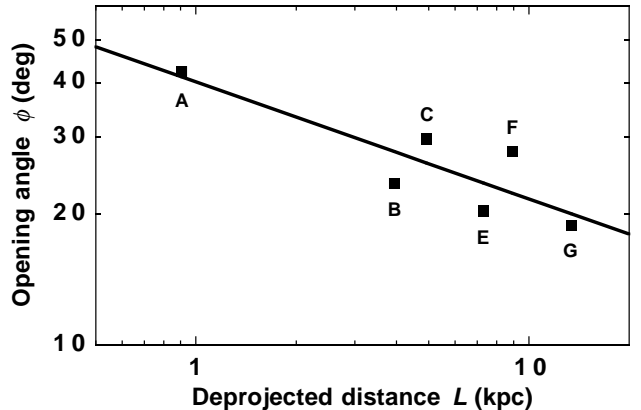


FIG. 1.— Opening angle of the Cen A jet (in the regions including the X-ray knots; labeled) ϕ vs. the deprojected distance from galactic core L . Here, the definition of $\phi = 2 \tan^{-1}(R \sin \theta / L_{\text{proj}})$ has been used, where R and L_{proj} are the radius of jet and projected distance from the core, respectively (cf. Table 3), and θ is the viewing angle, assumed to be 15° (Hardcastle et al. 2003). The solid line indicates the interpolation among the points.

tending to the radial direction (Honda & Honda 2004). The well-pronounced tail would have an ability to trap plasma, and this stuff is responsible for the observed edge-brightened features (mentioned in Section 1; Hardcastle et al. 2007). Relating to this, it is shown in Figure 1 that the jet opening angle tends to decrease as away from the core; this trend continues up to knot G. This observational fact seems to suggest that such a magnetic field certainly exerts the net collimation force for jet wide (Honda & Honda 2002), implying that the transverse correlation length of the magnetized filamentary turbulence reaches the radial size scale of the jet (beyond the aforementioned size scale of compact X-ray knots). Within the present framework, the various size scale of fragmented pieces inside the jet is considered to reflect the coherence length of the turbulence (as compatible with the argument given in Section 2.1), although the real situation might be more complicated (Blandford & Königl 1979a,b; Hardcastle et al. 2003).

Founded on this simple model, in the following Section 3 we attempt to expand rigorous arguments on the DSA of particles in the inner region ($\theta_{\text{proj}} \leq 60''$), in which the knots A and B have been, at least in part, associated with shock acceleration sites (Hardcastle et al. 2007). As the outer jet of $\theta_{\text{proj}} > 60''$ concerns, the X-ray emission is largely diffuse, and the compact knots embedded in the diffuse emission are much smaller than the radial sizes of the jet. Although there is no evidence for shocks (other than at knots) anywhere in the outer jet of $\theta_{\text{proj}} > 60''$ at the moment, it seems that the appearance of such inner structure as well as the measured X-ray spectrum can be explained by the present model including the inhomogeneity, according to the discussions given above. It is also noted that in the outer region, the presence of stochastic magnetic fields has been suggested (Mao & Wang 2007, within the framework of Fleishman (2006)). At this juncture, we provide, in the subsequent Section 4, a preliminary argument parallel to that ex-

panded in Section 3, considering an application of the model to the issue of particle acceleration in the outer region ($60'' < \theta_{\text{proj}} \leq 200''$) including knots C, E, F, and G, where magnetic self-collimation of the jet seems to be viable (Figure 1).

3. PARTICLE ACCELERATION IN THE INNER JET REGION

3.1. Acceleration Timescale

In the filamentary medium, the diffusion property of nuclei is quite different from that of electrons. For instructive manner, let us begin with considering the cold limit, in which any species of charged particles are gyrotrapped in the (local) mean magnetic field permeating through a filament. For the DSA in this regime, the particles will suffer conventional gyro-resonant diffusion, going back and forth across the shock discontinuity to gain their energies. Then, the mean acceleration time is roughly proportional to $\sim r_g/c$, where r_g is the gyro-radius (smaller than the radial size of the filament). In the ordinary case in which radiative mechanism spontaneously impedes particle energization, the kinetic energies disperse among the particle species, such that the ratio of the resulting gyro-radii among proton, arbitrary ion, and electron would indicate

$$r_{g,p} : r_{g,i} : r_{g,e} = 1 : \frac{1}{\sqrt{Z}} \left(\frac{A}{Z} \right)^2 : \left(\frac{m_e}{m_p} \right)^2, \quad (2)$$

respectively, where Z and A are the charge and mass number of nuclei, and $m_{e,p}$ is the electron and proton mass, respectively. That is, we read off $r_{g,p} \sim r_{g,i}$, and $r_{g,p}/r_{g,e} \sim O(10^6)$. The result indicates that the proton (ion) escape from magnetized filaments, which is associated with the bound-free transition (Honda & Honda 2005), is easier than the electron escape.

Unlike the major electrons quasi-secularly bound to the filaments (Section 2.1; Honda & Honda 2007; Honda 2008), energetic ions are likely to freely meander in the forest of filaments, undergoing the three-dimensional rms deflection. The latter is in the regime of the off-resonant scattering diffusion, which still makes possible to go back and forth across the shock, to additionally accelerate the transitionally injected ions to a higher energy range (Honda & Honda 2004, 2005). It is mentioned that this original idea could be reconciled with the recent simulation results for the similar plasma configuration (Section 2.1; Spitkovsky 2008).

When considering the ideal Fermi type-I mechanism, the energy spectral index of accelerated ions ought to be identical to that of co-accelerated electrons (see, e.g., Schlickeiser 2002, for details), and thus, denoted commonly as p . The mean acceleration time for arbitrary nuclei is found to be given by

$$t_{\text{acc}} \simeq \frac{\sqrt{6}\pi a_1(\beta, p) c}{8 R} \left(\frac{E}{ZeBU} \right)^2, \quad (3)$$

where a_1 is the dimensionless factor

$$a_1(\beta, p) = \frac{\beta(2p+1)}{(\beta-1)(p^2-1)}, \quad (4)$$

which is of order unity, and e , E , R , and U are the elementary charge, particle energy, (transverse) correla-

tion length of the filamentary turbulence, and flow speed upstream viewed in the shock rest frame, respectively (Honda & Honda 2005). Recalling the arguments given in Section 2.2, R is reasonably compared with the radius of the jet, rather than that of compact knots. It is noted that Equation (3) is valid for the unbound particles, which meander in the magnetized filaments, though still confined in the system with the size $\sim R$. Hereafter, we set $p = 2.4$, along with the arguments in Section 2.1. In this Section 3, we pay attention to the inner regions that wrap the well-resolved small X-ray knots AX1, AX2, AX3, AX4, BX2, and BX5 (Kraft et al. 2002; Kataoka & Stawarz 2005). For convenience, the parameter values (referred for the analysis in Section 3) are summarized in Table 1. Equation (3) is used to balance the various loss timescales evaluated below, to solve for E .

3.2. Temporal Limits

3.2.1. Shock-Accelerator Operation Time

The dynamical timescales concerning the energy limit of accelerated particles include the operation time of shock accelerator and adiabatic expansion loss time. It is hard to precisely evaluate the former, because of the difficulty of the identification of shock structure and U . In an ideal case in which the shock is stationary as sustained by an exhaustless incoming flow, one can ignore this kind of restriction, so that the maximum energy analysis can be simplified (the related discussion is given later). Below, we consider, for heuristic, the generic situation in which the shock accelerator moves along the jet. For simplicity, it may be reasonable to compare U to the moving speed (with respect to the core). The shock accelerator operation time can then be estimated as $t_{\text{sh}} \sim L/U$, and the adiabatic expansion loss time, $t_{\text{ad}} \sim 3L/(2U_r)$ (e.g., Mücke et al. 2003), where L and U_r are the length scale of the jet and the speed of radial expansion, respectively. For $U > U_r$ compatible with the self-collimating characteristic of jet flow (Section 2.2), we have the relation of $t_{\text{sh}} < t_{\text{ad}}$, which suggests that t_{sh} preferentially limits the particle acceleration.

When taking into account of the relativistic effects, the scaling of t_{sh} can be explicitly written as follows:

$$t_{\text{sh}} = 2.1 \times 10^{10} \frac{1}{\Gamma(U)} \frac{L}{1 \text{ kpc}} \frac{0.5c}{U} \text{ s}. \quad (5)$$

Here, $\Gamma = [1 - (U/c)^2]^{-1/2}$, and L is the deprojected distance of the concerned knotty regions from the core, that is, $L_{\text{proj}}/\sin \theta$, where L_{proj} and θ are the projected distance and viewing angle, respectively (Section 2.1). According to the discussions given above, we set $U = U_{\text{app}}/[\sin \theta + (U_{\text{app}}/c) \cos \theta]$, where U_{app} stands for the apparent speed of motion. In Figure 2, we plot t_{sh} as a function of θ , for the cases of $U_{\text{app}} = 0.1c$ (top) and $0.5c$ (bottom). It is noted that the enhancement of t_{sh} for the marginally smaller θ is due to the dominant increase of L against the increase of U and Γ in the right-hand side of Equation (5). For a plausible value of $\theta = 15^\circ$ (shaded lines; Hardcastle et al. 2003), one can find $t_{\text{sh}} \sim 10^{11} - 10^{12}$ s. For example, for a possible parameter set of $U_{\text{app}} = 0.1c$ and $\theta = 15^\circ$, we figure out $t_{\text{sh}} = 3.5 \times 10^{11}$ s and 1.5×10^{12} s in the regions with knots AX1 and BX5, respectively.

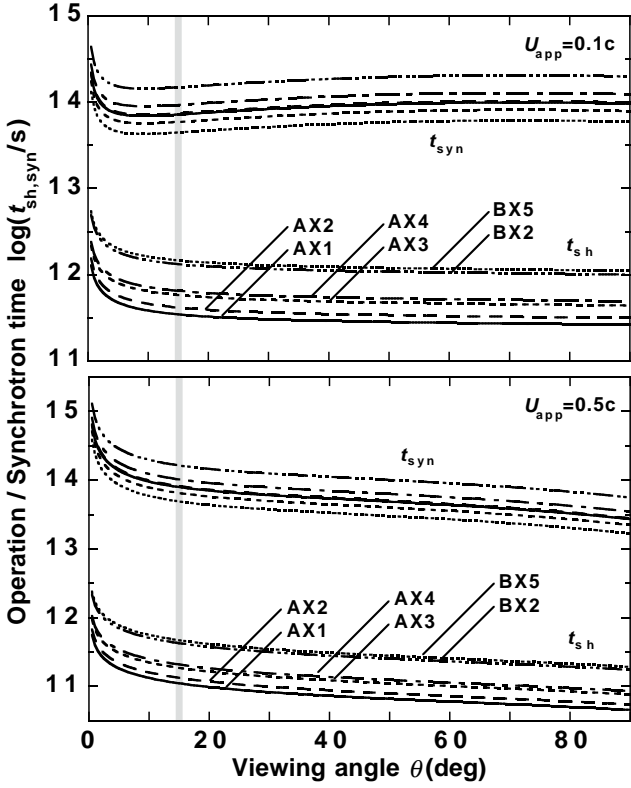


FIG. 2.— Operation timescales of shock accelerator t_{sh} for the apparent speed of $U_{app} = 0.1c$ (top) and $0.5c$ (bottom) vs. θ , in the regions around the six inner bright X-ray knots (included in the projection of $\theta_{proj} \leq 60^\circ$; labeled). The synchrotron cooling timescales t_{syn} are also indicated (the explanatory notes correspond to those for t_{sh}).

3.2.2. Radiative Losses

The radiative losses of the charged particles meandering in the filamentary medium compete with the energization. We anticipate that the emission is of diffuse (Fleishman 2006), and then, the cooling timescale that can be expressed as $t_{syn} = 36\pi^2 \tilde{\tau}(\beta)(A/Z)^4 [m_p^4 c^7 / (c^4 B^2 E)]$, where $\tilde{\tau}(\beta) = (6\pi)^{-2} [\beta(\beta + 2)^2(\beta + 3)] / [2\beta(\beta^2 + 7\beta + 8)]$ (Honda & Honda 2007). For the maximum energy analysis, the temporal balance of $t_{acc} = t_{syn}$ gives the solution of E , and putting this into the t_{syn} -expression denoted above is found to provide the following practical scaling

$$t_{syn} = 8.4 \times 10^{14} a_1(\beta, p)^{1/3} \left[\frac{\tilde{\tau}(\beta)}{10^{-3}} \right]^{2/3} \frac{1}{Z^{2/3}} \left(\frac{A}{2Z} \right)^{8/3} \times \left(\frac{100 \mu G}{B} \right)^2 \left(\frac{100 \text{ pc}}{R} \right)^{1/3} \left(\frac{0.5c}{U} \right)^{2/3} \text{ s.} \quad (6)$$

Note that setting to $(\beta, p) = (5/3, 2.4)$, which reflects $(\alpha_r, \alpha_x) = (0.7, 1)$ (cf. Section 2.1), gives $a_1 = 3.0$ and $\tilde{\tau} = 2.4 \times 10^{-3}$. In Equation (6), B is the quantity in the shock rest frame, and hence, for the moving shock case, set to $B_{eq, \delta=1} \delta^{-5/7}$ (Kataoka & Stawarz 2005), where $\delta = \Gamma^{-1} [1 - (U/c) \cos \theta]^{-1} (> 1)$ is the beaming factor,

and $U = U(U_{app}, \theta)$ (Section 3.2.1).

Relating to this loss process, here it might be useful to remark the collision with photons, which also limits the particle energization. This actually takes place, as far as a finite u_{rad} level is sustained by the synchrotron radiation from co-accelerated electrons, galactic emissions, not to mention cosmic background lights. The timescale of the $p\gamma$ interaction can be estimated as $t_{p\gamma} \sim (\chi \tilde{\tau})^{-1} (u_m/u_{rad}) t_{syn}$, where χ is a dimensionless factor almost independent of the source parameters (Biermann & Strittmatter 1987; Romero et al. 1996). By invoking $\chi \approx 200$, thereby $\chi \tilde{\tau} \lesssim O(1)$, we read off $t_{p\gamma} \gtrsim (u_m/u_{rad}) t_{syn}$, so that the inequality of $u_{rad} \leq u_m$, which is expected in the concerned jet-knot environments (Section 2.2), results in $t_{p\gamma} \geq t_{syn}$. It thus appears that for the maximum energy analysis, it is sufficient to balance $t_{acc} = t_{syn}$, as carried out above.

In Figure 2 for $U_{app} = 0.1c$ (top) and $0.5c$ (bottom), we show the t_{syn} levels for protons, i.e., Equation (6) for $(A, Z) = (1, 1)$, using the parameter values listed in Table 1. For smaller θ , t_{syn} sharply increases, since δ increases (i.e., B decreases). As θ increases, both δ and U decrease, so that their competition influences upon whether t_{syn} decreases or not in the larger θ -region. For the concerned regions, the timescale ranges from $t_{syn} = 4.5 \times 10^{13}$ s (BX5) to 1.5×10^{14} s (BX2) for $\theta = 15^\circ$. It is found that the t_{syn} level is order of magnitude higher than t_{sh} over the whole θ -range. As would be expected, the characteristic of the timescales well separated markedly simplifies the maximum energy analysis.

3.2.3. Collisional Loss

The collision of the cosmic-ray (test) particles with target particles also degrades the acceleration. In what follows, we clarify the condition for which the collisional loss can be neglected. The timescale of pp interaction may be simply given by $t_{col} = (\sigma_{pp} cn)^{-1}$, where $\sigma_{pp} \approx 4 \times 10^{-26}$ cm² and n are the cross section and number density of target protons, respectively. In conjunction with the issue of neutrino production, the pp collision involves the possible reaction channel of $p + p \rightarrow 2d + e^+ + \nu_e + \gamma$. Here we derive, for convenience, the critical density of target protons, denoted as n_{cr} , above which $t_{col} < \min(t_{sh}, t_{syn}) \sim t_{sh}$ sets in.

In Figure 3, we plot n_{cr} against θ . The $n_{cr}(\theta)$ depicted here is for the case of smaller $U_{app} = 0.1c$, since the value is lower (thereby, more crucial) than that for the larger U_{app} case. For the inclination of $\theta = 15^\circ$, the critical density ranges from 5.7×10^2 cm⁻³ (BX5) to $n_{cr} = 2.4 \times 10^3$ cm⁻³ (AX1). It turns out that, if $n < 10^2$ cm⁻³ is satisfied, t_{col} cannot be, in the whole θ -range, the shortest timescale among the energy loss processes. For example, the expected value of the order of $n \sim 10^{-1}$ cm⁻³ (Meisenheimer et al. 2007) leads to $t_{col} \gg \min(t_{sh}, t_{syn})$. That is to say, one can almost ignore the collisional effects on the energy loss. It follows that the pp neutrino production channel is less outweigh than the $p\gamma$ one that is considered in Section 3.5.

Summarizing the discussions in Section 3.2, we can claim that the temporal balance equation can be reduced as $t_{acc} = \min(t_{sh}, t_{syn}, t_{col}) \sim t_{sh}$, when considering the finite dynamical timescale of a moving shock. The solution for E is denoted as E_t , which indicates the maximum

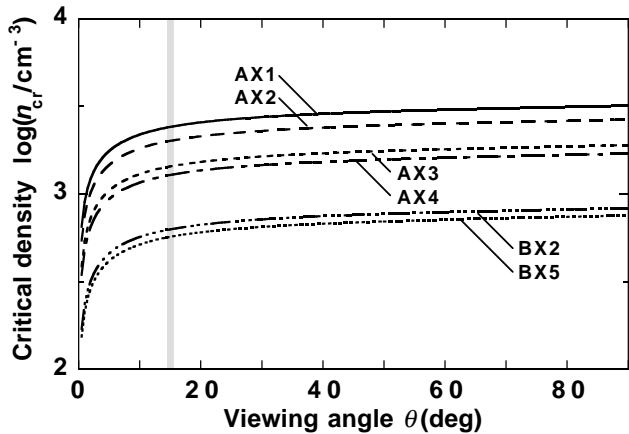


FIG. 3.— Critical density n_{cr} in each regions (labelled), above which the proton–proton collisional timescale t_{col} is shorter than t_{sh} (for $U_{app} = 0.1c$). For $\theta = 15^\circ$ (shaded line), it is evident that the collisional loss of an accelerated proton is less dominant, if $n < n_{cr} = 10^2 - 10^3 \text{ cm}^{-3}$.

possible energy of an accelerated particle, determined by the temporal limits. This value should be compared with the energy restricted from spatial scale; the related issue is discussed below.

3.3. Spatial Limit

In the present context, when the mean free path of accelerated particles, transverse to the filaments (λ_\perp), reaches the order of the radial size of the jet ($\sim R$), the particles would start escaping from the concerned system. This is just a subject to the spatial limit of particle acceleration. The balance equation $\lambda_\perp(E) = R$, contrast to $r_g = R$ for the conventional gyro-resonant DSA, appropriately provides the solution for E (denoted as E_s), which indicates the maximum possible energy determined by the spatial limit. Making use of the expression of λ_\perp that can be derived from the quasi-linear kinetic equation (see Honda & Honda 2005, for the details), we obtain

$$E_s = 4.3 \times 10^{18} a_2(\beta, p) Z \frac{B}{100 \mu\text{G}} \frac{R}{100 \text{ pc}} \text{ eV}, \quad (7)$$

where a_2 is the dimensionless factor

$$a_2(\beta, p) = \left[\frac{(\beta - 1)(p + 2)(p + 4)}{\beta} \right]^{1/2}. \quad (8)$$

Note that for $(\beta, p) = (5/3, 2.4)$, Equation (8) gives $a_2 = 3.4$.

If the outer ridge with the size exceeding R is pervaded by a large-scale magnetic tail (Section 2.2), we could speculatively regard such a size as effective confinement radius. When one allows for setting to , e.g., the value around $\sim R_{out} (> R)$ listed in Table 1 (Kraft et al. 2002), the E_s value (given in Equation (7)) is found to be raised by a factor of $\sim \sqrt{R_{out}/R}$. However, this factor is of the order unity, and it can be confirmed that the effect does not severely affect the conclusions for the

TABLE 2
THE MAXIMUM ENERGIES OF PROTON, IRON, AND NEUTRINO

Region	$E_{p,m}$ (EeV)	$E_{i,m}$ (ZeV)	$E_{\nu,m}$ (EeV)
AX1	35 (130)	0.92 (3.4)	1.8 (6.5)
AX2	38 (130)	0.99 (3.3)	1.9 (6.4)
AX3	50 (140)	1.3 (3.8)	2.5 (7.2)
AX4	43 (120)	1.1 (3.0)	2.1 (5.8)
BX2	64 (180)	1.7 (4.8)	3.2 (9.2)
BX5	120 (340)	3.2 (8.7)	6.1 (17)

NOTE. — Values in the round brackets indicate those for the stationary shock case.

simple case excluding them. In this aspect, here we show the analysis, for which Equation (7) is referred in the rather conservative manner, to provide the theoretical upper limit of particle energy which is of the form that can be made a direct comparison with E_t .

3.4. Highest Energies of Proton and Iron

For the concerned jet regions each, we evaluate the achievable maximum energy that is defined by $E_{max} = \min(E_s, E_t)$, where E_s is given by Equation (7), and E_t can be properly derived from $t_{acc} = t_{sh}$ as argued in Section 3.2, to have the scaling of

$$E_t = 2.1 \times 10^{19} \frac{1}{a_1(\beta, p)^{1/2}} Z \frac{B}{100 \mu\text{G}} \times \left(\frac{L}{1 \text{ kpc}} \right)^{1/2} \left(\frac{R}{100 \text{ pc}} \right)^{1/2} \left(\frac{U}{0.5c} \right)^{1/2} \text{ eV}. \quad (9)$$

Hereafter, the solutions E_{max} for proton (A, Z) = (1, 1) and iron (56, 26) are, for convenience, simply denoted as $E_{p,m}$ and $E_{i,m}$, respectively.

In Figure 4, for $Z = 1$ we plot E_s (Equation (7)) and E_t (Equation (9)), using the parameter values listed in Table 1. One can see that $E_{p,m} = \min(E_s, E_t) = E_t$ is ensured in the major range of $\theta > 5^\circ$, while in the marginally smaller θ , the spatial limit regime with $E_{p,m} = E_s$ can appear. Particularly, for a standard $\theta = 15^\circ$, it is sure that $E_{p,m} = E_t$ is valid for both $U_{app} = 0.1c$ and $0.5c$ in all concerned regions. This is one of the most noticeable results, which is different from the previous one derived from the analysis for a narrower jet with $R < 100 \text{ pc}$ (Vir A; Honda & Honda 2004), where $\min(E_s, E_t) = E_s$ appears in a possible U range. For practical reasons, the resulting values of $E_{p,m}$ for $U_{app} = 0.1c$ are listed in Table 2. It is noted that the U_{app} -dependence of $E_{p,m}$ is weak around $\theta = 15^\circ$, as seen in Figure 4. We can conclude that the $E_{p,m}$ value more likely reaches as high as $\sim 10^{20}$ eV in the inner jet region ($\theta \leq 60''$) including knots BX n . Also, the values of $E_{i,m}$ have been derived in parallel to $E_{p,m}$, and added in Table 2. It is found that the inner regions can be iron Zevatron; particularly, in the region with knot BX5, $E_{i,m}$ reaches 3.2×10^{21} eV.

Here, we provide the discussion on the special case in which the shock is stationary (Hardcastle et al. 2003). The operation of DSA continues until the incoming flow into the shock breaks off; otherwise, the accelerator secularly operates. In the former case, it is hard to determine t_{sh} , because of the complexity of the spatiotemporal dynamical evolution of the jet. For the present maximum energy analysis, it might be adequate for considering the

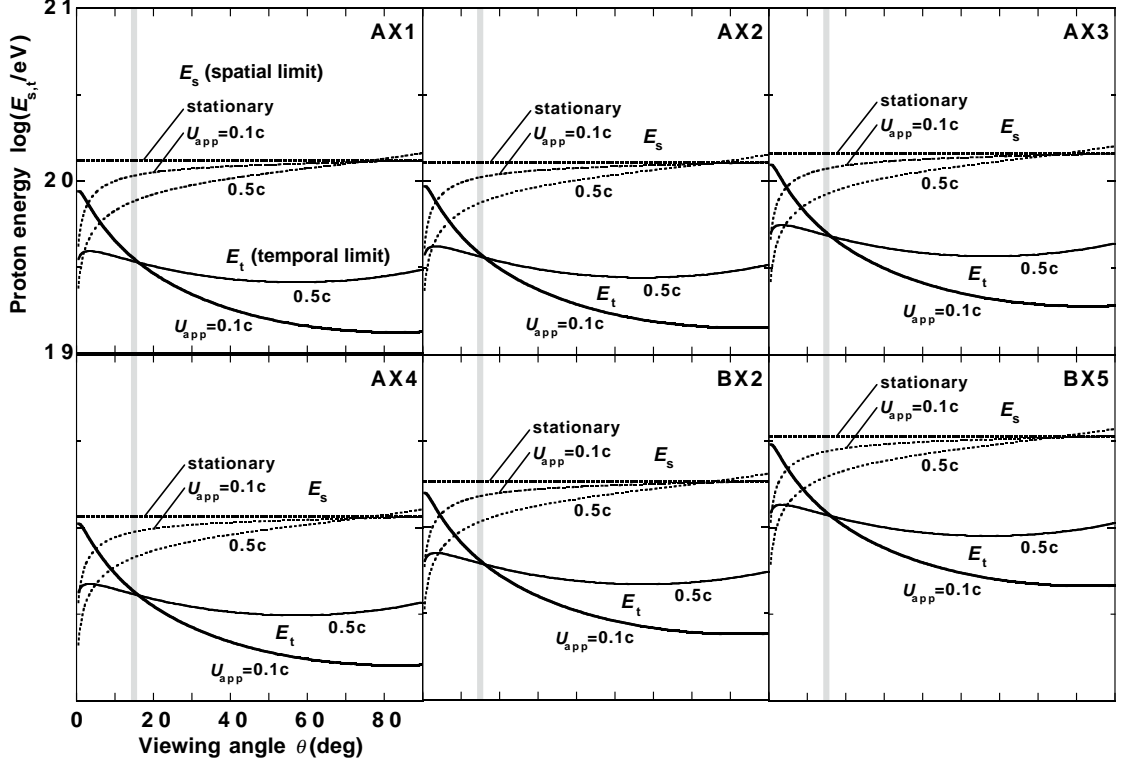


FIG. 4.— Proton energies E_s and E_t determined by the spatial and temporal limits, respectively, in each region (labeled). The axes are common in the panels. Note that $E_t(\theta)$ is the solution for $\min(t_{\text{sh}}, t_{\text{syn}}, t_{\text{col}}) = t_{\text{sh}}$, given U_{app} (labeled). The achievable maximum energy is given by $E_{\text{max}} = \min(E_s, E_t)$; for both $U_{\text{app}} = 0.1c$ and $0.5c$, $E_{\text{max}} = E_t$ is satisfied at $\theta = 15^\circ$ (shaded lines), and for the stationary shock case, $E_{\text{max}} = E_s$. The E_{max} values (denoted as $E_{m,p}$ for proton) are summarized in Table 2.

latter, and then, we read the temporal balance equation of $t_{\text{acc}} = \min(t_{\text{ad}}, t_{\text{syn}}, t_{\text{col}})$, which yields an enhanced value of E_t , such that $\min(E_s, E_t) = E_s$ more likely appears. The E_s -levels evaluated from Equation (7), set as $B = B_{\text{eq}, \delta=1}$, are indicated in Figure 4. For convenience, we list the resulting $E_{p,m}$ -values in Table 2 (in round brackets). In comparison with the results of $U_{\text{app}} = 0.1c$, the values of $E_{p,m}$ increase, since the E_s -values are larger than E_t (determined from E_{sh}), as seen in Figure 4.

The magnetic field strength involves the uncertainty, coming about through some assumptions in the estimation of the equipartition value (Section 2.2). Thus we also investigate the field intensity dependence of $E_{p,i,m}$. In Figure 5, we show $E_{p,m}$ against $B_{\text{eq}, \delta=1}$ for $\theta = 15^\circ$; the linear relations simply stem from $E_s/t \propto B (= B_{\text{eq}, \delta=1} \delta^{-5/7})$ in Equations (7) and (9). It is found that in the region with knot BX5, $E_{p,m}(E_{i,m}) \geq 10^{20}$ eV can be achieved for the ranges of $B_{\text{eq}, \delta=1} \geq 230 \mu\text{G}$ ($9 \mu\text{G}$) and $\geq 85 \mu\text{G}$ ($3 \mu\text{G}$) for $U_{\text{app}} = 0.1c$ and stationary shock cases, respectively.

3.5. High-energy Neutrino Emissions

The $p\gamma$ interaction discussed in Section 3.2.2 is revisited in light of the major neutrino production mechanism. The reaction sets in when the center of mass energy of a $p\gamma$ interaction exceeds the threshold energy for the Δ -resonance; that is, $E_{p,m}$ is required for ex-

ceeding the quantity of $(m_\Delta^2 - m_p^2)c^4/4E_\gamma$ ($\equiv E_{p,\text{th}}$), where m_Δ and E_γ are the mass of the Δ -particle and target photon energy, respectively (e.g., Halzen & Hooper 2002). The threshold energy is found to scale as $E_{p,\text{th}} = 1.6 \times 10^{17} \Gamma^2 (1 \text{ eV}/E_\gamma) \text{ eV}$. Above $E_{p,\text{th}}$, charged and neutral pions can be created by $p\gamma \rightarrow \Delta \rightarrow n\pi^+$ and $p\gamma \rightarrow \Delta \rightarrow p\pi^0$, and the former triggers the decay chain of $\pi^+ \rightarrow \mu^+ + \nu_\mu \rightarrow e^+ + \nu_e + \bar{\nu}_\mu + \nu_\mu$, to produce the very high energy neutrinos.

Provided that the four final state leptons in the decay chain equally share the pion energy, the threshold neutrino energy can be estimated as $E_{\nu,\text{th}} = \frac{1}{4} \langle x_{p \rightarrow \pi} \rangle E_{p,\text{th}}$, where $\langle x_{p \rightarrow \pi} \rangle$ is the average fraction of energy transferred from the initial proton to the produced pion (Halzen & Hooper 2002). By virtue of the active galactic nucleus (AGN) unification scheme (cf. Section 5; Urry & Padovani 1995; Tsvetanov et al. 1998), it might be justified to adopt the estimation of $\langle x_{p \rightarrow \pi} \rangle \simeq 0.2$, which is adequate for blazar jet environments. Then, for the target photon energy in the range of $E_\gamma \sim 1 \text{ eV}$ (for the Cen A jet; e.g., Hardcastle et al. 2006), we work out at $E_{\nu,\text{th}} \simeq 8 \times 10^{15} \text{ eV}$. Similarly, one can estimate the achievable maximum neutrino energy (denoted as $E_{\nu,m}$) with reference to the $E_{p,m}$ values obtained above. For convenience, the resultant $E_{\nu,m}$ values are listed in Table 2. We find that $E_{\nu,m}$ is likely to be of EeV range in the inner region; for $U_{\text{app}} = 0.1c$ and the stationary

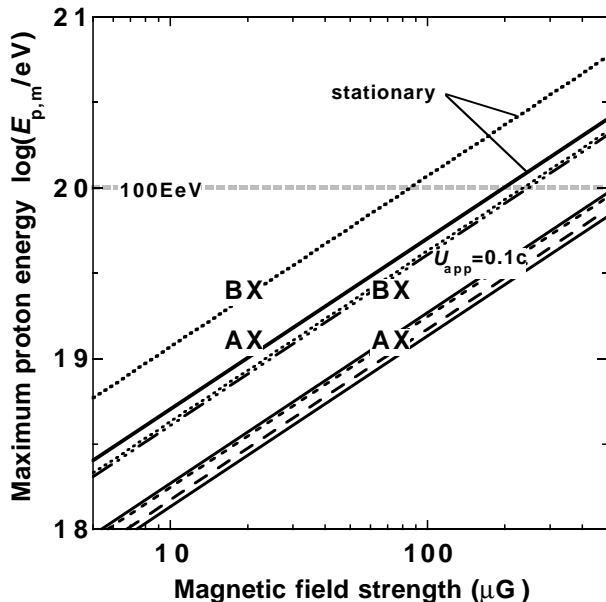


FIG. 5.— Maximum proton energy $E_{p,m}$ vs. the magnetic field strength compared to an equipartition value $B_{\text{eq},\delta=1} (= B\delta^{5/7})$, for $U_{\text{app}} = 0.1c$ and stationary shock cases. The explanatory notes for the former are the same as those given in Figures 2 and 3.

case, the uppermost value is expected to reach as high as 6×10^{18} eV and 2×10^{19} eV, respectively, in the region including knot BX5.

Concerning the observability of the neutrino flux (ϕ_ν) by a μ -scintillation counter with the conversion probability ($P_{\nu \rightarrow \mu}$), the number of detected events could be expressed as a function of neutrino energy, such that $N_{\text{events}} \sim \phi_\nu P_{\nu \rightarrow \mu} \propto E_\nu^{-1/2}$ (Halzen & Hooper 2002). Since we have little knowledge of the actual efficiency of energy conversion from accelerated protons to neutrinos in FR-I radio jets, the spectral normalization of ϕ_ν involves the large uncertainty. Considering the Auger flux, however, Cuoco & Hannestad (2008) attempted to calculate the neutrino event rate in the detectors like IceCube, and found a rate of $\sim 0.4 - 0.6 \text{ yr}^{-1}$ above a threshold of 10^{14} eV. In any case, the estimated $E_{\nu,m}$ provides the truncation energy of the neutrino spectrum, and in turn, could influence the neutrino flux estimation when the spectral index is given. The related issue is important for clarifying the share of cosmic-ray energy above the “knee” among celestial sources, but seems to be somewhat out of scope in this paper.

4. ON THE PARTICLE ACCELERATION IN THE LARGE-SCALE JET

4.1. Spatiotemporal Limits

It may be worth applying the present DSA scenario to the unsolved issue of particle acceleration in the outer region more distant from the galactic core. Here, we preliminarily show the E_{max} distribution in the large-scale jet, simply providing B as a parameter (without reference to the values given in Table 1), and spatial profile of n . This might be more meaningful, if the length

TABLE 3
SUMMARY OF THE PARAMETER AND E_{max} VALUES

Region	$L(\text{kpc})^a$	$R(\text{pc})^b$	β	$E_{p,m}(\text{EeV})^c$	$E_{i,m}(\text{ZeV})^c$
A	0.910	352	5/3	6.5 (25)	0.17 (0.66)
B	3.94	819	5/3	21 (59)	0.54 (1.5)
C	4.93	1310	2	33 (100)	0.85 (2.7)
E	7.29	1310	2	40 (100)	1.0 (2.7)
F	8.95	2120	2	56 (170)	1.5 (4.4)
G	13.4	2120	2	69 (170)	1.8 (4.4)

^aThe deprojected length, assuming the viewing angle of $\theta = 15^\circ$ (Kraft et al. 2002; Hardcastle et al. 2003).

^bcf. Kraft et al. (2002).

^cExplanatory note for the round brackets is the same as that in Table 2.

and radial scales of jet preferentially determine E_{max} , as we have seen this property in the inner region (Section 3). In the following, we investigate the condition, for which radiative and collisional losses are negligible, to complete the discussions on the feasibility of UHECR production in the large-scale jet up to $\theta_{\text{proj}} \simeq 200''$ ($L_{\text{proj}} \simeq 3.4$ kpc, including the outer knots C, E, F, and G; e.g., Kraft et al. 2002; Hardcastle et al. 2007).

For the analysis in Section 4, we adopt the parameter values listed in Table 3, with the use of the standard parameter set of $U_{\text{app}} = 0.1c$ and $p = 2.4$. We assume $\beta = 5/3$ in the inner region including knots A and B, and $\beta = 2$ in the outer region including knots C, E, F, and G, according to the arguments of the filamentary turbulent states (Section 2.1): in Equations (7) and (9), for instance, the latter case $(\beta, p) = (2, 2.4)$, which reflects $(\alpha_r, \alpha_x) = (0.7, 1.2)$, gives $a_1 = 2.4$, $a_2 = 3.8$, and $\tilde{\tau} = 4.3 \times 10^{-3}$.

In Figure 6, we plot t_{sh} and t_{syn} , that is, Equation (5) for given θ as a parameter, and Equation (6) with $(A, Z) = (1, 1)$ and $(56, 26)$, given $B_{\text{eq},\delta=1}$ as a parameter (while $\theta = 15^\circ$ fixed). It is clearly seen that as L_{proj} increases, the value of t_{sh} monotonically increases; especially for $\theta = 15^\circ$, from $t_{\text{sh}} = 3.2 \times 10^{11}$ s (knot A) to 4.7×10^{12} s (knot G). Note that the self-consistently determined t_{syn} level for iron is comparable with that for proton, reflecting the physics that in the original timescale (being proportional to $(A/Z)^4 E^{-1}$), the enhancement by the factor of $(A/Z)^4$ for iron is nearly canceled by the increase of E , which is caused by both the weaker synchrotron loss and stronger acceleration efficiency (on account of the reduced $t_{\text{acc}} \propto 1/Z^2$). Anyhow, it appears that, as far as the possible condition of $B_{\text{eq},\delta=1} \leq 500 \mu\text{G}$ is retained, t_{sh} is smaller than t_{syn} in the entire region including knots A–G.

As for the collisional loss, in parallel with the argument in Section 3.2.3, we provide the critical proton density n_{cr} , above which $t_{\text{col}} < t_{\text{sh}}$ sets in. For the timescale of nucleus–proton (Np) collision with $t_{\text{col}} \sim (\sigma_{Np}cn)^{-1}$, we recall an empirical scaling of the cross section of $\sigma_{Np} \sim \pi r_0^2 A^{2/3}$, where $r_0 \approx 1.4 \times 10^{-13}$ cm. In Figure 7, we explicitly depict n_{cr} against L_{proj} for pp and Np (say, $A = 56$) collisions, for the case of $\theta = 15^\circ$. The level of n_{cr} for Np is lower than that for pp , simply reflecting the thing that t_{col} for Np is shorter than for pp (by the factor of ~ 0.04). The value of n_{cr} decreases as L_{proj} increases; e.g., for the pp case, it ranges from $n_{\text{cr}} \simeq 3 \times 10^3 \text{ cm}^{-3}$ (knot A) to $2 \times 10^2 \text{ cm}^{-3}$ (knot G).

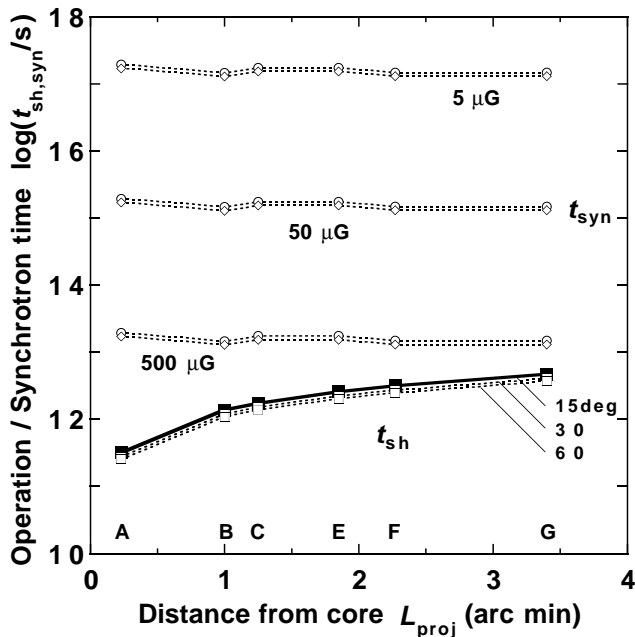


FIG. 6.— t_{sh} for given θ (labeled) and t_{syn} for given $B_{eq, \delta=1}$ (labeled) in each regions (labeled); up to the projected distance of $\sim 200''$ from the core). The open circles and diamonds indicate t_{syn} for proton (A, Z) = (1, 1) and iron (56, 26), respectively (providing $\theta = 15^\circ$). Note that $t_{sh} < t_{syn}$ is satisfied for the conceivable ranges of θ and $B_{eq, \delta=1}$ throughout the concerned regions.

Here, we attempt to make an ad hoc comparison with a density distribution deduced from the beta model that reasonably describes the galactic structure (Kraft et al. 2002). By reasoning that the jet matter is concentrated on the opening angle of ϕ ($\sim 2R/L$; i.e., the solid angle of $\pi\phi^2/4$), we invoke the crude density profile (along the jet) of $n(L_{proj}) \sim (16/\phi^2)n_b(r)$, where $L_{proj} = r \sin \theta$ and $n_b = n_0[1 + (r/r_G)^2]^{-3b/2}$ is the beta-model density. In Figure 7, we exemplify the density profile of $n = 10^2 n_b$, reflecting $\theta = 15^\circ$ and $\phi \sim 20^\circ$ (Figure 1). Here, the parameter values of $n_0 = 4.0 \times 10^{-2} \text{ cm}^{-3}$, $r_G = 0.5 \text{ kpc}$, and $b = 0.4$, have been adopted (Kraft et al. 2002). We then find that n takes the value in the range of $\sim 10^{-1} - 10^0 \text{ cm}^{-3}$ in between the region of knot A to G (in accord with a value suggested by Meisenheimer et al. (2007)), and the level is order of magnitude lower than the n_{cr} level for both the pp and Np collisions. Thus, it is claimed that the collisional effects on the energy limit are negligible. As a consequence, we can expect the significant reduction of $\min(t_{sh}, t_{syn}, t_{col}) \sim t_{sh}$, so that the temporal balance of $t_{acc} = t_{sh}$ provides the correct solution for E_t .

4.2. Highest Energies

For each regions in the large-scale jet, we evaluate the achievable maximum energy of proton/iron, defined by $E_{p/i,m} = \min(E_s, E_t)$, where E_s and E_t are given by Equations (7) and (9), respectively. In Figure 8, we plot E_s and E_t (for $Z = 1$ and 26), providing $\theta = 15^\circ$ and $B_{eq, \delta=1} = 50 \mu\text{G}$ (Romero et al. 1996; Israel 1998; Hard-

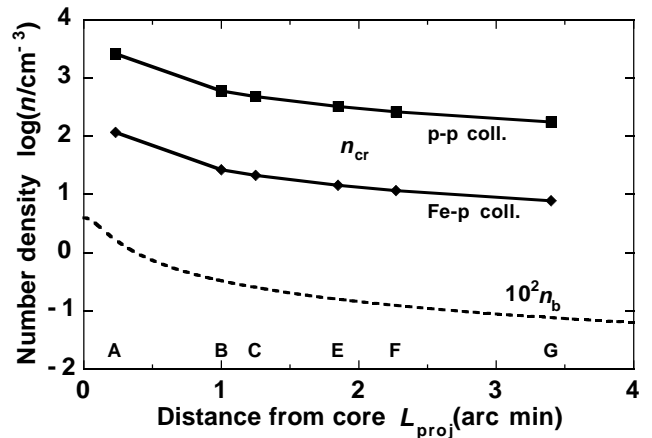


FIG. 7.— Critical density n_{cr} in each regions (labeled), above which $t_{col} < t_{sh}$ (for $U_{app} = 0.1c$), for the proton-proton and iron-proton collision cases (labeled). For a comparison, the profile of the beta-model density n_b , multiplied by factor 10^2 , is also depicted (short dashed) as a function of L_{proj} . For further explanation, see the text.

castle et al. 2006; Meisenheimer et al. 2007) throughout the concerned regions. The assumption of the $B_{eq, \delta=1}$ value, which corresponds to a spatially averaged one, is adequate for the present purpose, although the actual value might be larger, particularly, in the inner jet region (Section 2.2). One can see that $\min(E_s, E_t) = E_t$ is satisfied as a whole, for both proton and iron. The values of $E_{p/i,m}$ are summarized in Table 3. It seems more likely that, in the outer jet region, $E_{p,m}$ can hardly reach $\sim 10^{20} \text{ eV}$, even though setting R -value to the uppermost range, whereas $E_{i,m}$ exceeds 10^{20} eV , and reaches up to $2 \times 10^{21} \text{ eV}$. When considering the stationary shock (in parallel to the arguments in Section 3), the $E_{p/i,m}$ value increases, and particularly, $E_{p,m} \sim 10^{20} \text{ eV}$ is achieved in the outer region. With regard to the neutrino production via the photopionization decay chains, we read off $E_{\nu,m} = \frac{1}{4} \langle x_{p \rightarrow \pi} \rangle E_{p,m} \gtrsim 10^{18} \text{ eV}$ in the outer region. Although the obtained results are preliminary, involving parameter dependency, the expected overall features can be reconciled with the manifestation (given in Sections 3.4 and 3.5) that the Cen A jet is a candidate for the UHE proton accelerator that serves as EeV neutrino factory, and simultaneously, for the iron Zevatron.

5. DISCUSSION AND CONCLUSIONS

The validity of the filamentary model has been checked by reproducing the complicated blazar variabilities that involve the non-monotonous hysteresis patterns of broadband electromagnetic spectrum in flare phases (Honda 2008). By recalling the idea that regards FR-I radio sources as misaligned BL Lac objects (Urry & Padovani 1995; Tsvetanov et al. 1998), the application of the filamentary model to the Cen A jet will be reasonably justified. As for the particle acceleration in the filamentary medium, we point out that the present DSA mechanism for nuclei, which owes to the (off-resonant) three-dimensional rms diffusion across the shock (Section 3.1),

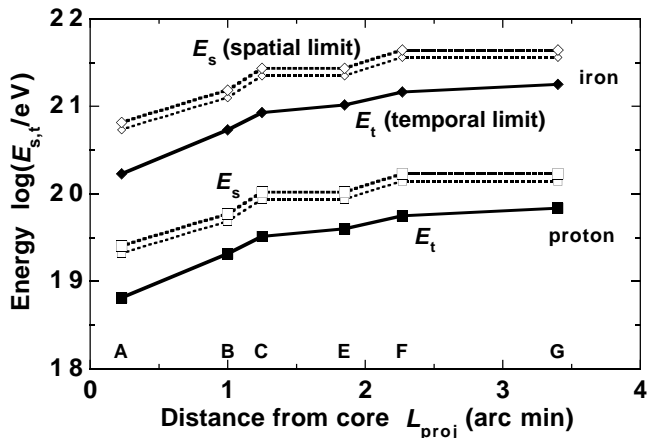


FIG. 8.— Energies E_s (open marks) and E_t (filled marks) determined by the spatial and temporal limits, respectively, for proton and iron acceleration (labeled). Here, $\theta = 15^\circ$ and $B_{\text{eq}, \delta=1} = 50 \mu\text{G}$ have been assumed throughout the concerned regions (labeled). The filled marks indicate the maximum energy obtained as $E_{\text{max}} = \min(E_s, E_t) = E_t$ for $U_{\text{app}} = 0.1c$, where E_s is indicated by the smaller marks; and the (larger) open ones indicate $E_{\text{max}} = E_s$ for the stationary shock case. The E_{max} values (denoted as $E_{m,p}$ and $E_{m,i}$ for proton and iron, respectively) are summarized in Table 3.

is simpler than the electron acceleration mechanism that is incorporated with the complexity of the energy hierarchy mediated by the transition injection (Honda & Honda 2007). The acceleration of highest energy particle in the Cen A was first considered by Romero et al. (1996). In the early work, they dealt with the conventional gyro-resonant diffusion model even for proton, that is to say, implicitly supposed a large-scale ordered magnetic field (with small-amplitude perturbations). They addressed that a proton could be accelerated to the energy of 2.7×10^{21} eV in situ, which is an order of magnitude larger than the present $E_{p,m}$ values that are in the range of $\sim 10^{19} - 10^{20}$ eV (Section 3.4; Table 2). Such a larger value was derived from simply equating a classical acceleration timescale (e.g., Biermann & Strittmatter 1987) with radiative loss timescales, but this fashion now appears to be somewhat optimistic (Section 3.2.2; Figure 2). It can be claimed that taking into account of the shock operation time or particle escape is essential for the maximum energy analysis for the concerned source, to yield the reduced proton energy, which can hardly reach the 10^{21} eV energy range. It is also mentioned that the situation in which the dynamical timescale limits the particle acceleration is analogous to the situation that typically appears in the supernova remnant shock

acceleration, in which the adiabatic expansion of spherical shell likely becomes a major loss mechanism (e.g., Kobayakawa et al. 2002).

In conclusion, we have evaluated the achievable maximum energies of the proton and iron nucleus diffusively accelerated by the shock in the Cen A jet including X-ray knots. In particular, we have taken into account of the more realistic DSA scenario that relies on the filamentary jet model responsible for the recent X-ray measurements, and elaborated the conceivable energy restriction stemming from spatiotemporal scales. The key finding is that, for the plausible ranges of the shock speed of $\sim 0.1c$, viewing angle of $\gtrsim 10^\circ$, and magnetic intensity of $\lesssim 500 \mu\text{G}$, the uppermost particle energy tends to be inevitably limited by the shock accelerator operation timescale ($< 10^{13}$ s), rather than the radiative cooling losses ($\gtrsim 10^{13}$ s). As a result, it has been demonstrated that there exists the acceleration region (off the galactic core), in which proton and iron can be energized to $\sim 10^{20}$ eV and $\sim 10^{21}$ eV ranges, respectively. In particular, for the inner region including the X-ray knot BX5, we work out at the maximum energies of 1×10^{20} eV and 3×10^{21} eV for proton and iron, respectively; and estimate the corresponding cutoff energy of the neutrino produced via the photopionization, as 6×10^{18} eV. For the stationary shock case, we can expect the enhancement of the maximum energies, and read that the large-scale region up to the projection of about $200''$, as well, has a potential to energize proton and iron beyond 10^{20} eV and 10^{21} eV, respectively, to yield the $p\gamma$ neutrino with the energy exceeding 5×10^{18} eV. We here manifest that the jet wide of the Cen A galaxy is a promising candidate for the UHE proton accelerator and Zevatron for high- Z nucleus, as desirable to account for the outcome from the Auger observatory (Abraham et al. 2007).

The derived large values of particle energies are of those achievable at the acceleration sites. The observable energies ought to be, of course, reduced, due to a major energy loss mechanism including the photopion interaction with cosmic microwave background. However, the Cen A is so nearby that the ballistic transport is anticipated to be not crucially degraded, on account of the weak decay property (such as $-(1/E)(dE/dt) \sim 10^{-8} \text{ yr}^{-1}$ for $E > 10^{20}$ eV; Romero et al. (1996)). We hope, in near future, the application of the present scenario to cosmologically distant (super GZK) AGNs, to solidify the point source scenario for dominant UHECR production, which is responsible for the suppression of cosmic-ray flux above 4×10^{19} eV that has recently been confirmed by the Auger's experiments (Abraham et al. 2008), and also, is of interest in conjunction with the detection of super GZK neutrinos (e.g., Ringwald 2006).

I am grateful to Y. S. Honda for a useful discussion.

REFERENCES

- Abraham, J., et al. (The Pierre Auger Collaboration) 2007, *Science*, 318, 939
 Abraham, J., et al. (The Pierre Auger Collaboration) 2008, *Phys. Rev. Lett.*, 101, 061101
 Aharonian, F., et al. 2009, *ApJ*, 695, L40
 Bai, J. M., & Lee, M. G. 2001, *ApJ*, 549, L173
 Biermann, P. L., & Strittmatter, P. A. 1987, *ApJ*, 322, 643
 Blandford, R. D., & Eichler, D. 1987, *Phys. Rep.*, 154, 1
 Blandford, R. D., & Königl, A. 1979a, *ApL*, 20, 15
 Blandford, R. D., & Königl, A. 1979b, *ApJ*, 232, 34
 Brookes, M. H., Lawrence, C. R., Keene, J., Stern, D., Gorjian, V., Werner, M., & Charmandaris, V. 2006, *ApJ*, 646, L41
 Cuoco, A., & Hannestad, S. 2008, *Phys. Rev. D*, 78, 023007
 Evans, D. A., Kraft, R. P., Worrall, D. M., Hardcastle, M. J., Jones, C., Forman, W. R., & Murray, S. S. 2004, *ApJ*, 612, 786

- Ferrarese, L., Mould, J. R., Stetson, P. B., Tonry, J. L., Blakeslee, J. P., & Ajhar, E. A. 2007, *ApJ*, 654, 186
- Fleishman, G. D. 2006, *MNRAS*, 365, L11
- Greisen, K. 1966, *Phys. Rev. Lett.*, 16, 748
- Halzen, F., & Hooper, D. 2002, *Rep. Prog. Phys.*, 65, 1025
- Hardcastle, M. J., Cheung, C. C., Feain, I. J., & Stawarz, L. 2009, *MNRAS*, 393, 1041
- Hardcastle, M. J., Kraft, R. P., & Worrall, D. M. 2006, *MNRAS*, 368, L15
- Hardcastle, M. J., Worrall, D. M., Kraft, R. P., Forman, W. R., Jones, C., & Murray, S. S. 2003, *ApJ*, 593, 169
- Hardcastle, M. J., et al. 2007, *ApJ*, 670, L81
- Honda, M. 2004, *Phys. Rev. E*, 69, 016401
- Honda, M. 2008, *ApJ*, 675, L61
- Honda, M., & Honda, Y. S. 2002, *ApJ*, 569, L39
- Honda, M., & Honda, Y. S. 2004, *ApJ*, 617, L37
- Honda, M., & Honda, Y. S. 2005, *ApJ*, 633, 733
- Honda, M., & Honda, Y. S. 2007, *ApJ*, 654, 885
- Honda, M., Meyer-ter-Vehn, J., & Pukhov, A. 2000a, *Phys. Plasmas*, 7, 1302
- Honda, M., Meyer-ter-Vehn, J., & Pukhov, A. 2000b, *Phys. Rev. Lett.*, 85, 2128
- Horiuchi, S., Meier, D. L., Preston, R. A., & Tingay, S. J. 2006, *PASJ*, 58, 211
- Israel, F. P. 1998, *A&AR*, 8, 237
- Kataoka, J., & Stawarz, L. 2005, *ApJ*, 622, 797
- Kataoka, J., Stawarz, L., Aharonian, F., Takahara, F., Ostrowski, M., & Edwards, P. G. 2006, *ApJ*, 641, 158
- Kobayakawa, K., Honda, Y. S., & Samura, T. 2002, *Phys. Rev. D*, 66, 083004
- Kraft, R. P., Forman, W. R., Jones, C., Murray, S. S., Hardcastle, M. J., & Worrall, D. M. 2002, *ApJ*, 569, 54
- Lobanov A. P., & Zensus J. A. 2001, *Science*, 294, 128
- Mao, J., & Wang, J. 2007, *ApJ*, 669, L13
- Markowitz, A., et al. 2007, *ApJ*, 665, 209
- Medvedev, M. V., & Loeb, A. 1999, *ApJ*, 526, 697
- Meisenheimer, et al. 2007, *A&A*, 471, 453
- Mücke, A., Protheroe, R. J., Engel, R., Rachen, J. P., & Stanev, T. 2003, *Astropart. Phys.*, 18, 593
- Owen, F. N., Hardee, P. E., & Cornwell, T. J. 1989, *ApJ*, 340, 698
- Perley, R. A., Dreher, J. W., & Cowan, J. J. 1984, *ApJ*, 285, L35
- Piner, B. G., Pant, N., Edwards, P. G., & Wiik, K. 2009, *ApJ*, 690, L31
- Ringwald, A. 2006, *J. Phys. Conf. Ser.*, 39, 393
- Romero, G. E., Combi, J. A., Perez Bergliffa, S. E., & Anchordoqui, L. A. 1996, *Astropart. Phys.*, 5, 279
- Schlickeiser, R. 2002, *Cosmic Ray Astrophysics* (Berlin: Springer)
- Spitkovsky, A. 2008, *ApJ*, 682, L5
- Stanev, T. 2008, arXiv:0805.1746
- Swain M. R., Bridle A. H., & Baum S. A. 1998, *ApJ*, 507, L29
- Trichel K., Rudnick L., Hardcastle M. J., & Leahy J. P. 2001, *ApJ*, 561, 691
- Tsvetanov, Z. I., Hartig, G. F., Ford, H. C., Dopita, M. A., Kriss, G. A., Pei, Y. C., Dressel, L. L., & Harms, R. J. 1998, *ApJ*, 493, L83
- Urry, C. M., & Padovani, P. 1995, *PASP*, 107, 803
- Vallée, J. P. 2004, *New Astron. Rev.*, 48, 763
- Zatsepin, G. T., & Kuzmin, V. A. 1966, *J. Exp. Theor. Phys. Lett.*, 4, 78